

Active transpressional tectonics in the Andean forearc of southern Peru quantified by 10 Be surface exposure dating of an active fault scarp

Carlos Benavente, Swann Zerathe, Laurence Audin, Sarah R Hall, Xavier Robert, Fabrizio Delgado, Julien Carcaillet, A.S.T.E.R. Team

▶ **To cite this version:**

Carlos Benavente, Swann Zerathe, Laurence Audin, Sarah R Hall, Xavier Robert, et al.. Active transpressional tectonics in the Andean forearc of southern Peru quantified by 10 Be surface exposure dating of an active fault scarp. Tectonics, 2017, 36 (9), pp.1662-1678. 10.1002/2017tc004523 . hal-03135850

HAL Id: hal-03135850
https://hal.science/hal-03135850

Submitted on 9 Feb 2021

HAL is a multi-disciplinary open access archive for the deposit and dissemination of scientific research documents, whether they are published or not. The documents may come from teaching and research institutions in France or abroad, or from public or private research centers.

L'archive ouverte pluridisciplinaire **HAL**, est destinée au dépôt et à la diffusion de documents scientifiques de niveau recherche, publiés ou non, émanant des établissements d'enseignement et de recherche français ou étrangers, des laboratoires publics ou privés.

AGU PUBLICATIONS

Tectonics

RESEARCH ARTICLE
10.1002/2017TC004523

*ASTER Team: Georges Aumaître, Didier L. Bourlès, and Karim Keddadouche.

Key Points:
- A new 60 km long active transpressional-fault is evidenced in the southern Peruvian forearc
- ^{10}Be cosmic ray exposure dating and morphological observations suggest recurrent seismic events in the last thousands of years
- Significant amount of crustal deformation may accumulate on discrete faults within the Andean forearc

Supporting Information:
- Supporting Information S1
- Data Set S1

Correspondence to:
S. Zerathe,
swann.zerathe@ird.fr

Citation:
Benavente, C., S. Zerathe, L. Audin, S. R. Hall, X. Robert, F. Delgado, J. Carcaillet, and ASTER Team (2017), Active transpressional tectonics in the Andean forearc of southern Peru quantified by ^{10}Be surface exposure dating of an active fault scarp, *Tectonics*, *36*, doi:10.1002/2017TC004523.

Received 21 FEB 2017
Accepted 24 JUL 2017
Accepted article online 28 JUL 2017

©2017. American Geophysical Union. All Rights Reserved.

Active transpressional tectonics in the Andean forearc of southern Peru quantified by ^{10}Be surface exposure dating of an active fault scarp

Carlos Benavente[1,2], Swann Zerathe[1,2], Laurence Audin[2], Sarah R. Hall[3], Xavier Robert[1,2], Fabrizio Delgado[1], Julien Carcaillet[2], and ASTER Team[4]*

[1]Instituto Geológico, Minero y Metalúrgico INGEMMET, San Borja, Peru, [2]Université Grenoble Alpes, Université Savoie Mont Blanc, CNRS, IRD, IFSTTAR, ISTerre, Grenoble, France, [3]Environmental Science, College of the Atlantic, Bar Harbor, Maine, USA, [4]Aix-Marseille Université, CNRS-IRD-Collège de France, UM 34 CEREGE, Technopôle de l'Environnement Arbois-Méditerranée, Aix-en-Provence, France

Abstract Our understanding of the style and rate of Quaternary tectonic deformation in the forearc of the Central Andes is hampered by a lack of field observations and constraints on neotectonic structures. Here we present a detailed analysis of the Purgatorio fault, a recently recognized active fault located in the forearc of southern Peru. Based on field and remote sensing analysis (Pléiades DEM), we define the Purgatorio fault as a subvertical structure trending NW-SE to W-E along its 60 km length, connecting, on its eastern end, to the crustal Incapuquio Fault System. The Purgatorio fault accommodates right-lateral transpressional deformation, as shown by the numerous lateral and vertical plurimetric offsets recorded along strike. In particular, scarp with a 5 m cumulative throw is preserved and displays cobbles that are cut and covered by slickensides. Cosmogenic radionuclide exposure dating (^{10}Be) of quartzite cobbles along the vertical fault scarp yields young exposure ages that can be bracketed between 0 to 6 ka, depending on the inheritance model that is applied. Our preferred scenario, which takes in account our geomorphic observations, implies at least two distinct rupture events, each associated with ~3 and ~2 m of vertical offset. These two events plausibly occurred during the last thousand years. Nevertheless, an interpretation invoking more tectonic events along the fault cannot be ruled out. This work affirms crustal deformation along active faults in the Andean forearc of southern Peru during the last thousand years.

1. Introduction

While the Andean range is cited as a typical example of an active mountain belt associated with subduction processes, the mechanics of its growth and deformation are still subject to ongoing debate [e.g., *Isacks*, 1988; *McQuarrie*, 2002; *Armijo et al.*, 2015]. Although the style, distribution, timing, and rates of crustal deformation are well documented in the subandean domain of the eastern Andean flank [e.g., *McGroder et al.*, 2015; *Rocha and Cristallini*, 2015, and references therein], the literature contains few data along the Andean forearc. In the Central Andean forearc, two opposing models suggest either (1) a simple subduction interface between a plunging oceanic slab and a continental forearc accommodating little to no modern deformation [e.g., *Uyeda and Kanamori*, 1979; *Isacks*, 1988] or (2) the presence of localized faults accommodating part of the deformation by active tectonics that contribute to relief development [*Audin et al.*, 2006; *Hall et al.*, 2008; *Schildgen et al.*, 2009; *Armijo et al.*, 2015].

For several reasons, crustal fault activity ($<$10 mm yr^{-1}) [*Hall et al.*, 2012] in the Andean forearc cannot be documented by GPS monitoring [*Chlieh et al.*, 2011]. The forearc sits above the seismically coupled megathrust, implying that present-day crustal deformation field is dominated by elastic deformation (10 to 40 mm yr^{-1} along the coast) due to the subduction seismic cycle; the sole opportunity to document fault activity at Quaternary time scales is provided by tectonic geomorphology studies [*Audin et al.*, 2003; *Saillard et al.*, 2017; *Riesner et al.*, 2017]. Previous studies have argued that records of tectonic activity are limited to Andean forearc landscape features of southern Peru [e.g., *Sébrier et al.*, 1985]; however, more recent studies have not only shown that active structures exist and accommodate relief growth but have also suggested that rates based on dated offset geomorphic features should also be considered in models of recent forearc deformation [e.g., *Hall et al.*, 2012].

In compressional forearc settings, near-surface fault expressions are often blind, associated with folded Quaternary sediments or abrupt changes in topography. In turn, river incision rates can be interpreted as

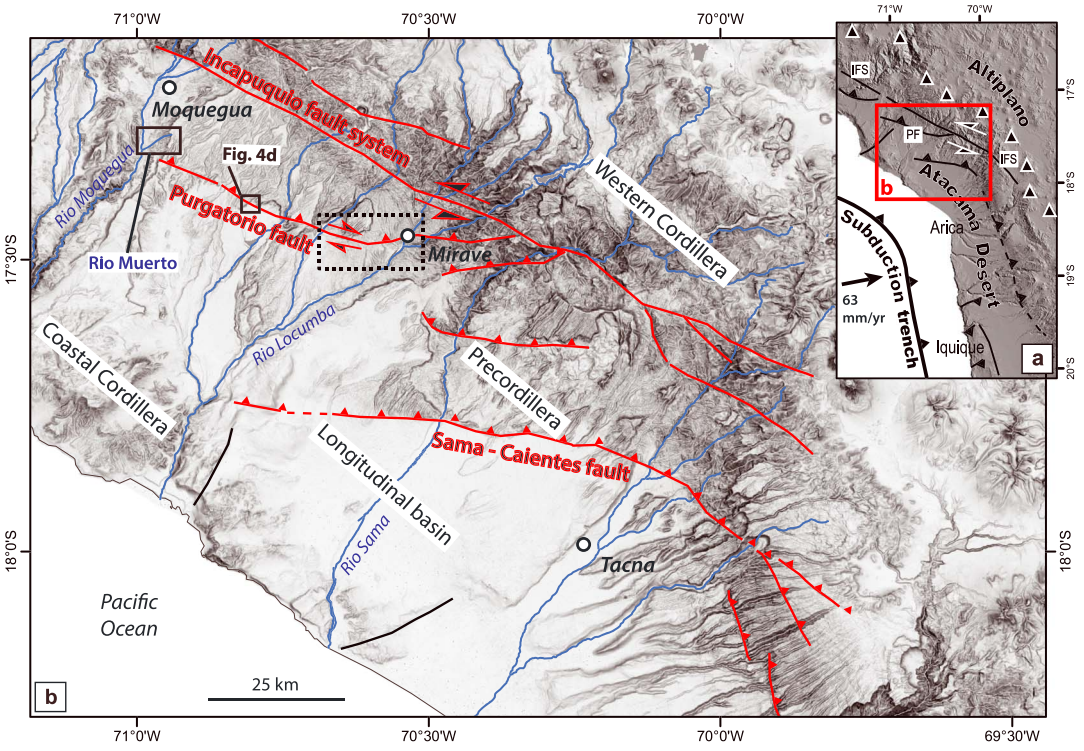


Figure 1. Active tectonic context of the southern Peruvian forearc. (a) The Andean forearc along the Arica Bend (i.e., the coastal flexure) depicting the major fault systems. The arrow indicates the relative plate motion of Nazca/South America [*Chlieh et al.*, 2011]: PF and IFS stand for Purgatorio Fault and Incapuquio Fault System, respectively. The black triangles indicate the location of volcanoes. (b) Structural map of southern Peru with the main faults including the Purgatorio and the Incapuquio active fault systems superimposed on a shaded relief image. The dashed black rectangle shows the boundary of the Pleiades images shown in Figure 2.

fault uplift rates [*Hall et al.*, 2012; *Alvarado et al.*, 2014], but this requires taking into account the effects of both climate variations and transient processes that remain mostly unknown [e.g., *Saillard et al.*, 2014; *Rolland et al.*, 2017]. Globally, only a few cases exist for which precise fault slip rates have been successfully determined by *direct* dating of a fault scarp [e.g., *Jackson et al.*, 2002]. In the Andes, despite recent updates of the active fault maps [e.g., http://neotec-opendata.com; http://geocatmin.ingemmet.gob.pe/geocatmin], no *direct* quantification of the timing of active fault activity has been proposed.

This study focuses on the 60 km long active Purgatorio Fault (PF), which has been recently documented in the Andean forearc of southwestern Peru (Figure 1a) [*Audin et al.*, 2006; *Hall et al.*, 2008]. This transpressive fault is a part of the active flower structure of the main Incapuquio Fault System (IFS) (Figure 1b) and disrupts the pediment surfaces within the arid Atacama landscape. Among the main EW-striking neotectonic faults of the forearc (Figure 1), the PF provides the clearest geomorphic evidence of recent activity [*Hall et al.*, 2008]. In particular, the PF shows a fresh vertical scarp of up to 5 m high with a free face, vertically offset alluvial terraces, and horizontally offset gullies. This setting offers a rare opportunity to understand how deformation may be localized within the central Andean forearc and to make observations that allow potential convergence partitioning to be assessed. To that end, we performed (1) an along-strike morphotectonic study based on field mapping of the structure and remote high-resolution digital elevation model (DEM) analysis and (2) direct ^{10}Be surface exposure dating of the fault scarp along a vertical profile to constrain the fault scarp age and to track fault slip rate.

2. Geologic and Tectonic Settings

2.1. The Western Andean Forearc

The study area is in southwestern Peru at ~17°S latitude, within the tectonically active forearc of the Andean Orogen where ongoing subduction of the Nazca Plate occurs at a rate of ~63 mm yr^{-1} [*Chlieh et al.*, 2011].

Quaternary shortening rates of the order of 10 to 15 mm yr^{-1} are estimated across the entire Central Andes [*Sébrier et al*., 1988; *Hindle et al*., 2002]. Geodetic studies show slower present-day shortening rates of about 4 to 9 mm yr^{-1} east of the Altiplano Plateau [*Bevis and Martel*, 2001]. In the study region of the southern Peruvian forearc, Pleistocene uplift rates of 0.2 to 0.4 mm yr^{-1} have been derived from cosmogenic dating of fluvial and marine terraces [*Saillard et al*., 2011; *Hall et al*., 2012], while longer term protracted uplift is deduced from thermochronology [e.g., *Schildgen et al*., 2009] or studies of geomorphic evolution [e.g., *Audin et al*., 2008; *Coudurier-Curveur et al*., 2015; *Armijo et al*., 2015]. However, no Quaternary or present-day shortening rates have been reported from this region of southwestern Peru.

Several geomorphic zones, trending parallel to the trench, define the forearc region: a Coastal Cordillera, a low-relief remnant landscape comprising the Precordillera and longitudinal basin in the pampas (northern Atacama Desert), and the Western Cordillera (Figure 1b). A striking characteristic of this area in southern Peru and northern Chile is the extreme aridity that has prevailed for several million years [*Dunai et al*., 2005]. Due to this long-lived hyperaridity, the regional landscape experienced extremely low denudation rates ($<$0.5 m Ma^{-1}), as supported by several cosmogenic nuclide studies (*Hall et al*. [2008, 2012] in southern Peru and *Dunai et al*. [2005], *Kober et al*. [2007], and *Placzek et al*. [2010] in northern Chile), allowing long-term preservation of the geomorphology. The exceptional preservation of landscape features allows for the recognition of several discrete transpressional fault systems affecting the Precordillera [*Audin et al*., 2003] (http://neotec-opendata.com; http://geocatmin.ingemmet.gob.pe/geocatmin). These faults accommodate mainly trenchward-vergent (~south) motion and connect along strike and at depth to the NW-SE lithospheric IFS in the east [*Jacay et al*., 2002].

2.2. The Purgatorio Fault System

The PF extends for 60 km between the town of Mirave in the east and the Moquegua valley in the west (Figure 1b). This area is underlain by Miocene sedimentary rocks, which are limited to the north-east by the IFS. Low-relief surfaces within this part of the Atacama Desert are built upon the late Miocene-Pliocene indurated conglomerates of the Moquegua Group [*Roperch et al*., 2006]. While the PF has a very youthful morphology, particularly along this segment, no historical surface ruptures, instrumental seismicity ($M_w > 4$), nor historical earthquakes have been reported [*Dorbath et al*., 1990].

3. Methodology

3.1. Field and High-Resolution DEM Analysis

To investigate the tectonic imprint of the PF both at the regional and local scales, we combine geomorphic observations based on field data with analyses of Google Earth images and high-resolution digital elevation models (DEMs). A new high-resolution DEM was derived from two stereo images acquired by the Pléiades satellites on 20/10/2015. The full resolution of these optical images is 0.7 m, and their orientation was assessed using the rational polynomial coefficient provided in their ancillary data. We generated the DEM using the open source software Ames Stereo Pipeline developed by NASA [*Broxton and Edwards*, 2008] and followed the three-step procedure described by *Lacroix* [2016]. First, each image was first map-projected using the low-resolution (30 m) Shuttle Radar Topography Mission DEM. Then the two images were bundle-adjusted based on automatically extracted tie points, before finding the disparities. The third step involved finding the intersection of all the rays coming from the homologous points of the image pair. This step leads to a point cloud of the surface topography, which is then converted onto a 2 m resolution grid. Using this high-resolution DEM, we mapped the fault and identified vertical and horizontal offsets of fluvial landscape features along the trace (Figure 2a). We conducted field campaigns to validate the observations and interpretations made based on our interpretation of the DEM and to map, sample, and perform field-based structural measurements along the exhumed fault scarp.

3.2. Cosmogenic ^{10}Be Dating

Cosmogenic-nuclide-based surface-exposure dating has been widely applied to determine the style and rates of tectonic deformation at the Earth's surface [e.g., *Benedetti and Van Der Woerd*, 2014, and references therein]. The method, based on the accumulation of cosmogenic nuclides (e.g., ^{10}Be, ^{36}Cl and ^{3}He) within the lattice of minerals (e.g., quartz, calcite and pyroxene), allows us to determine the exposure age of a rock at the Earth's surface [*Gosse and Phillips*, 2001]. Applications to constrain fault activities are abundant in

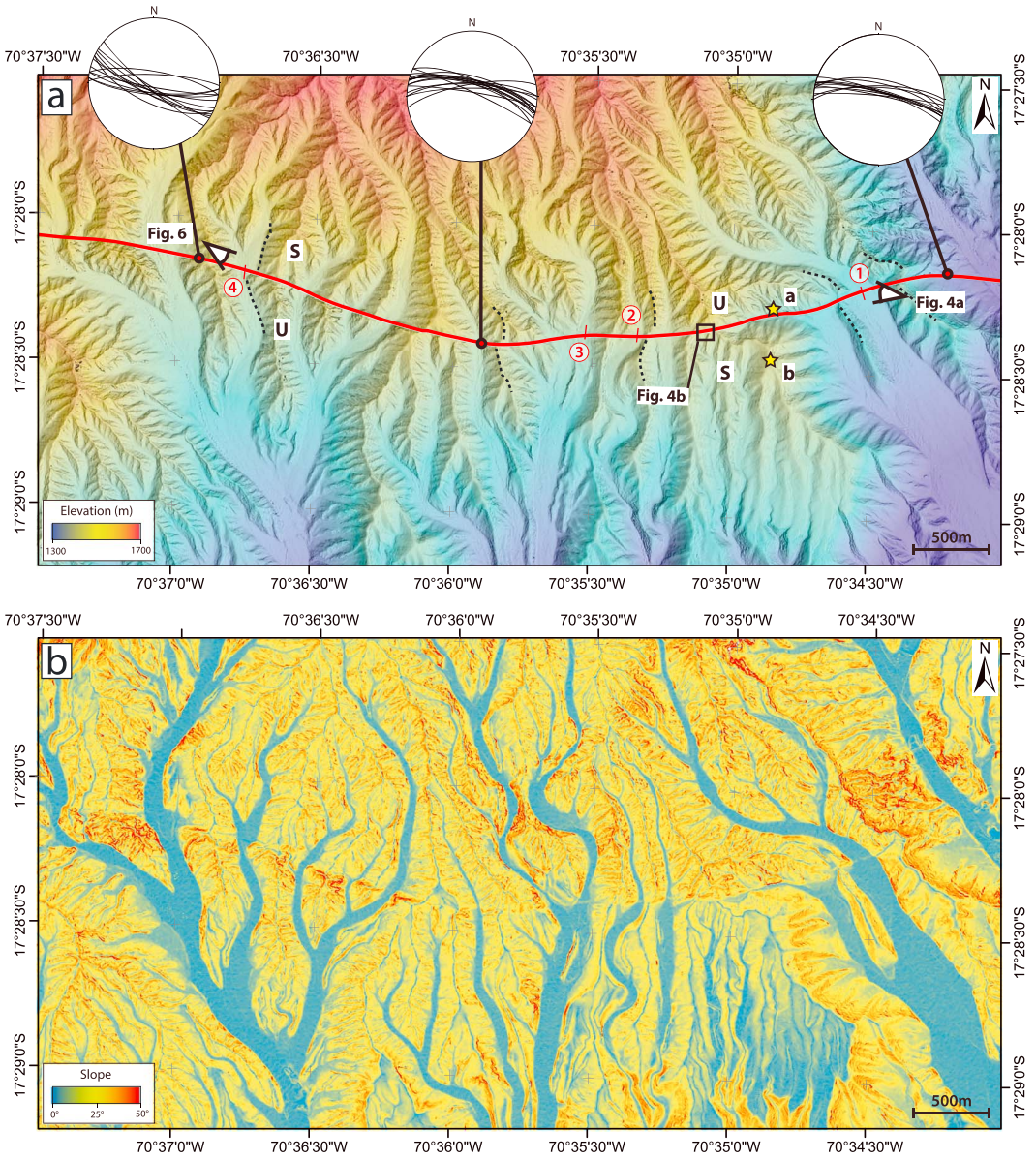


Figure 2. Topography surrounding the eastern segment of the Purgatorio Fault derived from the Pléiades DEM. (a) Hillshade image with fault plane measurements (stereoplots) located with the red points along the fault trace. The dashed black lines highlight examples of cumulative right-lateral offsets visible along ridge crests and valley flanks. The yellow stars indicate the location of the cosmogenic nuclide sampling sites with (a) corresponding to samples from this study and (b) from *Hall et al.* [2008] (see location on Figure 4a also). The circled numbers indicate the positions of topographic profiles shown on Figure 7. (U) and (S) stand for "Uplifted" (hanging wall) and "Subsided" (footwall) blocks, respectively. (b) Slope map. As the fault trace is clearly visible trending west to east across the center of the image, we have not highlighted it to allow for an unaltered view of the image.

the literature; they either focus on *direct* dating of exhumed fault scarps [*Benedetti et al.*, 2013] or on *geomorphic* assessment of deformation rates by dating tectonically offset landforms [e.g., *Jackson et al.*, 2002; *Chevalier et al.*, 2012; *Hetzel*, 2013]. Generally, studies that focus on dating fault scarps aim to identify (one or several) discrete event(s), as with paleoseismological trenching [e.g., *Perea et al.*, 2003]. Because scarps often preserve only a few events, it is difficult to determine long-term tectonic slip rates from these features; mapping and dating offset geomorphic markers is a preferred method for establishing slip rates over longer time scales [e.g., *Chevalier et al.*, 2012]. Nevertheless, in tectonically active regions with low deformation rates, the maximum slip rate compares in general with the rate that may be inferred from

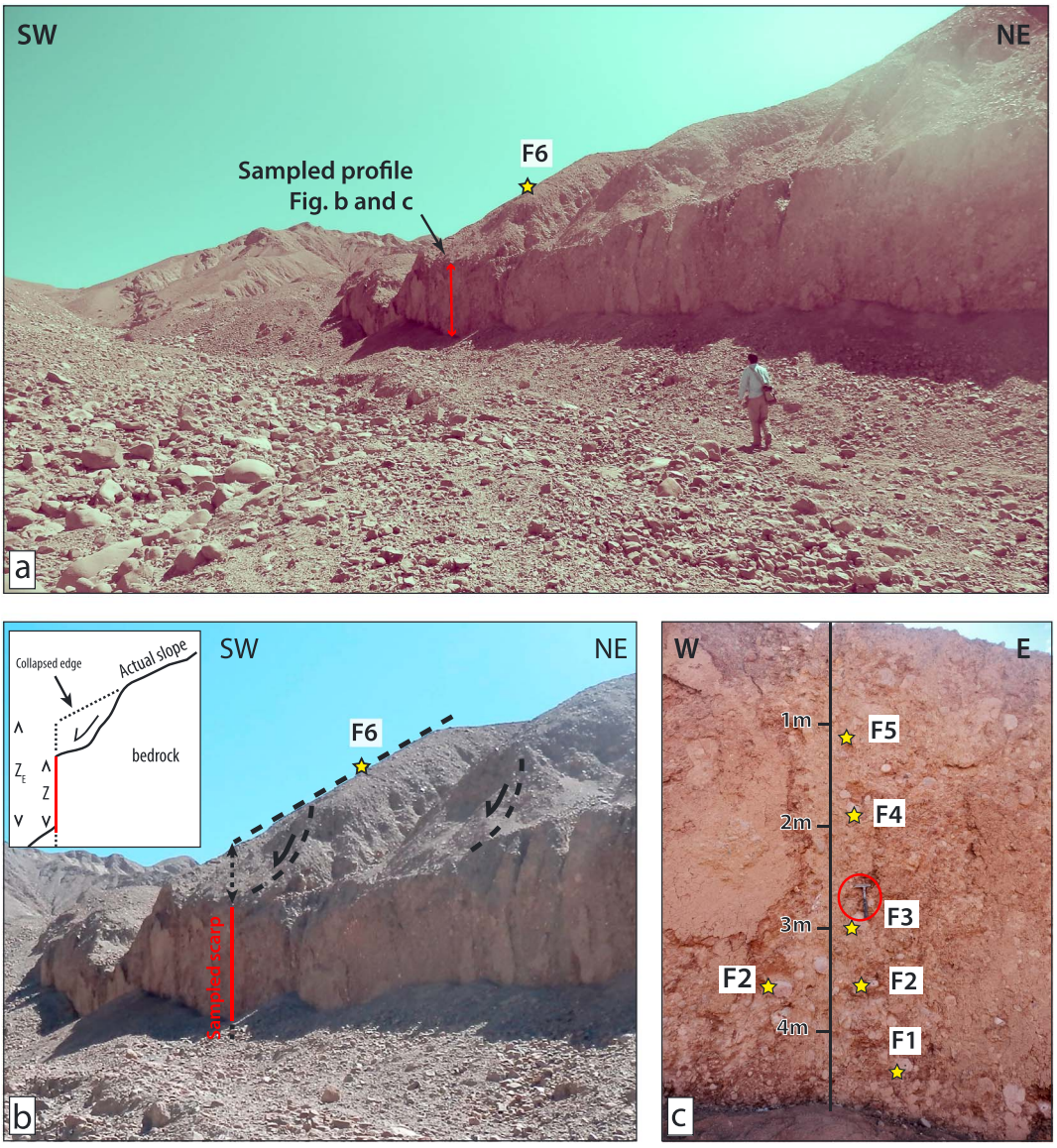


Figure 3. Sampling of the exhumed fault scarp (see location in Figures 2 and 4a). (a) Panoramic view with location of the sampled profile and sample F6 collected for denudation-rate measurement along the bedrock slope above the fault. Note the person for scale. (b) Zoom on the fault free-face, showing the collapse that affected the top of the scarp and showing how Z_E was estimated. (c) Zoom on the fault scarp where the yellow stars highlight the sampled cobbles. A hammer, circled in red above sample F3, provides an additional scale for reference.

trench data across the fault zones and from the slip associated with the past $M_w > 7$ earthquakes [*Baize et al.*, 2015]. In the case of the PF, datable and correlated offset geomorphic markers were hard to find, but its well-preserved near-vertical scarp (Figure 3) allows in situ dating along a vertical profile spanning several meters.

3.2.1. Sampling

To our knowledge this study is the first to attempt direct exposure-age dating of a fault scarp affecting a bedrock conglomerate. This approach was possible here because the conglomerates are extremely well indurated and contain pebbles and cobbles that are directly cut and striated along vertical surfaces by the fault, a guarantee that we sampled the original fault scarp. However, the low abundance of quartz-bearing cobbles prevented us from sampling at regular intervals (tens of centimeters) along the scarp, as is routinely done on calcareous fault scarps [e.g., *Benedetti et al.*, 2013]. Instead, we searched for the most suitable profile exposing a maximum number of quartz-bearing cobbles with sufficient diameters (>5 cm, Figure 3). We

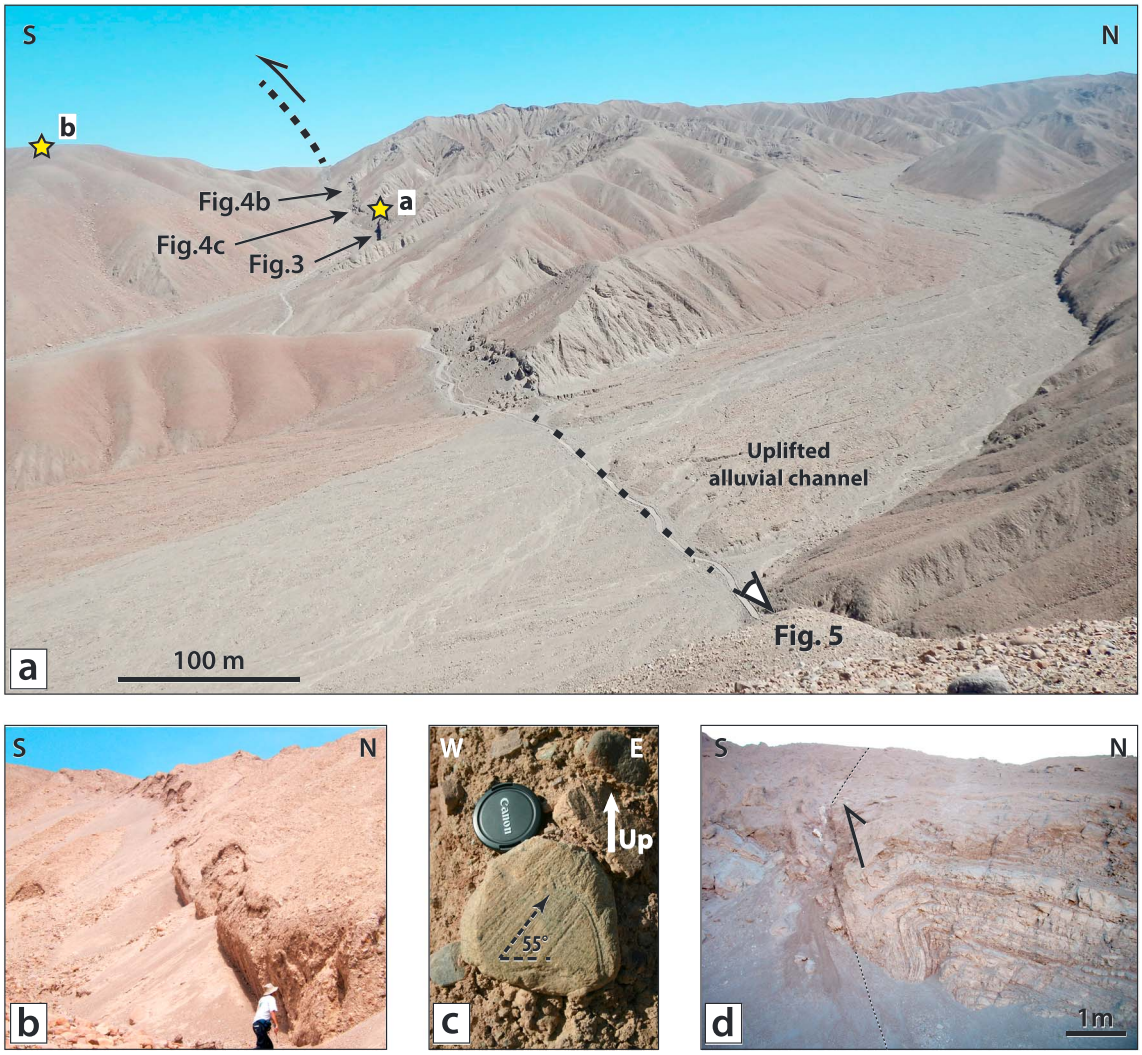


Figure 4. Field evidence for recent activity along the Purgatorio Fault (see location of photographs on Figures 1 and 2a). (a) Panoramic view. Here the fault crosses a fluvial channel (the fault trace is depicted by a dashed line) where its last activity resulted in an ~1.5 m uplift of the alluvial deposits in the active channel on the hanging wall (see also Figure 5). Striking differences in surface morphologies are visible on the two sides of the fault due to the differential erosion of the ascending and subsiding blocks. (b) Zoom on the reverse fault scarp locally oriented 095/80 N. (c) Slickensides imprinted on a cut cobble along the fault scarp. Here the rake dips ~55° toward the west and indicates oblique reverse movement. (d) Fault plane and anticlinal folds affecting sedimentary layers of the hanging wall (Moquegua layers) provide evidence of a compressional component along the fault (see location on Figure 1).

collected five samples along an ~3 m high profile (Figure 3c, see location in Figures 2a and 4a) by systematically selecting cobbles that were clearly cut by the fault and covered with tectonic slickensides on their cut face. Because cobbles from point F2 along the profile (Figure 3c) were very small, we sampled at two different points at the same horizontal level and mixed the two. Cobbles were brought back to the laboratory and cut with a circular saw to remove the buried portion and to control sample thickness.

When sampling, we recorded the distance of samples (Z) from the top of the scarp using a decameter. However, the geomorphology clearly shows that slumps have affected the top of the scarp (Figures 3a and 3b), implying that the distance Z does not correspond to the real sample depth below the surface before they were coseismically exhumed. Estimation of this preexhumation depth is crucial to account for inheritance; i.e., the amount of cosmogenic nuclides that were produced and accumulated in the samples at depth prior to surface exposure [*Gosse and Phillips*, 2001; *Zerathe et al.*, 2013, 2014]. The preexhumation depth (Z_E) was estimated by interpolating the scarp plane and the plane of the mean local topographic slope above (see sketch on Figure 3b). It suggests that about 3 m of the scarp top has collapsed before being subsequently exhumed

by a tectonic event. The fact that the vertical scarp height is very consistent along strike (Figure 3a) strengthens the interpretation that the slumps might predate the most recent exhumation.

To determine the inherited nuclide concentration, we must constrain the local long-term denudation rate of the topography. Therefore, a sample (F6) was collected from the sloping bedrock surface of the hanging wall, about 10 m above the fault-scarp (Figure 3a). We selected a quartz-bearing cobble extracted directly from the indurated conglomeratic Moquegua Fm (~Miocene) bedrock. Three loose cobbles collected by *Hall et al*. [2008] from a partially preserved pediment surface, about 250 m to the south of our sampling site (Figures 2 and 4a and Table 1), were also used to derive comparative long-term denudation rates from the footwall landscape.

3.2.2. ^{10}Be Measurements, Exposure Age, and Denudation Rate Calculations

Samples were prepared at the Centre Européen de Recherche et d'Enseignement des Géosciences de l'Environnement (CEREGE) (Aix-en-Provence, France) for measurement of in situ produced cosmogenic ^{10}Be concentrations from the quartz mineral fraction. We followed routine procedures, adapted from *Brown et al*. [1991] and *Bourles et al*. [1989], to purify the quartz and extract beryllium. The ^{10}Be concentrations were measured at the French AMS (accelerator mass spectrometry) national facility ASTER (Accélérateur pour les Sciences de la Terre, Environnement, Risques) [*Arnold et al*., 2013] at CEREGE laboratory, where ^{10}Be data were calibrated against the National Institute of Standards and Technology standard reference material 4325 by using an assigned ^{10}Be/^{9}Be ratio of 2.79 ± 0.03 * 10^{-11} [*Nishiizumi et al*., 2007]. Analytical uncertainties include the counting statistics, the machine stability (~0.5%) [*Arnold et al*., 2010], and the blank correction.

To derive denudation rates and exposure ages from the measured cosmogenic nuclide concentrations, we used the new MATLAB®-based CRONUScalc program, developed by *Marrero et al*. [2016] on the basis of the *Balco et al*. [2008] code. This program has the advantage of a straightforward method of calculation, approved by the community, and reflects the currently accepted practices in the field, thereby facilitating comparison and/or recalculation of results [*Phillips et al*., 2016]. We applied a globally calibrated ^{10}Be production rate of 3.92 ± 0.31 atm gr^{-1} yr^{-1} at sea level and high latitude [*Borchers et al*., 2016; *Phillips et al*., 2016]. This production rate was scaled at the geographical and altitudinal location of the sampling site using the LSDn (SA) flux-based and nuclide-dependent scaling-model of *Lifton et al*. [2014], which incorporates past magnetic field fluctuations and yielded favorable calibration results [*Borchers et al*., 2016; *Marrero et al*., 2016]. Atmospheric pressure at the sampling site was derived from the ERA-40 atmosphere model [*Uppala et al*., 2005]. We applied a density estimate of 2.6 g cm^{-3} for the bedrock conglomerates and an attenuation length of 160 g cm^{-2} for the neutron component [*Dunne et al*., 1999].

We initially calculated long-term denudation rates for the hanging wall surface based on the nuclide concentration of sample F6 (this study) and the footwall surface based on samples PG05-08, PG05-09, and PG05-19 (recalculated from *Hall et al*. [2008]) using the code "be10erate" of the CRONUScalc program (Table 1).

Second, we calculated the expected inheritance along the sampled fault scarp. Indeed, while the fault scarp is exposed at the surface at present, we must take into account that it resided at a shallow depth prior to fault rupture. During this period, all samples buried at depth along the future fault scarp were exposed to cosmic rays passing through the bedrock, slowly accumulating a cosmogenic nuclide abundance that is referred to as "inheritance." Therefore, the actual measured nuclide concentrations of the sampled cobbles are theoretically the sum of both the inherited concentration and the postexhumation concentration (accumulated during direct exposure); neglecting the inherited concentration could introduce bias in the age results [see *Zerathe et al*., 2013, 2014].

The inheritance is theoretically a function of (1) the long-term surface denudation rate that represents erosion from above, (2) the depth below the surface, and (3) the material density [*Lal*, 1991]. This was estimated using the MATLAB code "predN1026depth" available in the CRONUScalc program. We modeled two different surface denudation scenarios each of which produces a theoretical depth-concentration curve. In the first scenario, we applied the local hanging wall denudation rate of 13 ± 2 mm ka^{-1} derived from this study (sample F6, Table 1), and in the second, we used the denudation rate of the footwall (3–5 mm ka^{-1}) calculated from the data of *Hall et al*. [2008].

Finally, to obtain the concentration corresponding to a sample's surface exposure age, the inherited nuclide concentration modeled for the sampled depth was subtracted from the sample's measured ^{10}Be

AGU Tectonics

10.1002/2017TC004523

Table 1. Cosmogenic ^{10}Be Data and Field Parameters[a]

Sample	Latitude (S°)	Longitude (W°)	Elevation (m asl)	Z (m)	Z_E (m)	S	T (cm)	Mass (g)	Sn	Sμ	^{10}Be/^{9}Be (10^{-13})	^{10}Be[b] (10^4 at g^{-1})	Inheritance Scenario 1[c] (10^4 at g^{-1})	Inheritance Scenario 2[d] (10^4 at g^{-1})	Exposure ages (ka ± 1σ) for different scenarii[e]		
															No Inheritance	Scenario 1 ε = 13 mm ka^{-1}	Scenario 2 ε = 3–5 mm ka^{-1}
F1	17.47161	70.58085	1428.3	4.3	8.30	0.493	4	7.54	1.836	1.309	8.37	1.47 ± 0.14	1.46 ± 0.10	2.20	5.0 ± 0.4 (0.8)	0.7 ± 0.5 (0.7)	NaN
F2	17.47161	70.58085	1427.5	3.5	7.50	0.493	4	3.58	1.836	1.309	5.92	1.74 ± 0.23	1.55 ± 0.11	2.37	5.7 ± 0.6 (0.9)	0.7 ± 0.5 (0.6)	NaN
F3	17.47161	70.58085	1426.9	2.9	6.90	0.493	4	4.92	1.836	1.309	7.28	1.83 ± 0.21	1.62 ± 0.12	2.50	5.9 ± 0.5 (0.8)	0.7 ± 0.4 (0.5)	NaN
F4	17.47161	70.58085	1425.8	1.8	5.80	0.493	5	19.20	1.836	1.309	20.87	1.96 ± 0.14	1.75 ± 0.13	2.74	6.3 ± 0.4 (0.8)	0.7 ± 0.3 (0.5)	NaN
F5	17.47161	70.58085	1425.2	1.2	5.20	0.493	5	12.43	1.836	1.309	15.33	2.05 ± 0.26	1.82 ± 0.14	2.89	6.4 ± 0.7 (1)	0.2 ± 0.2 (0.3)	NaN
														Denudation rate (m.Ma^{-1})			
F6[f]	17.47168	70.58097	1440	–		0.919	4	6.18	1.93	1.923	111.05	35.97 ± 1.10		13 ± 2			
PG08[g]	17.47392	70.58092	1504	–		1	4	–	2.02	1.975	–	96.6 ± 0.3		5 ± 1			
PG09[g]	17.47392	70.58092	1504	–		1	4	–	2.02	1.975	–	97.7 ± 0.3		5 ± 1			
PG19[g]	17.47392	70.58092	1504	–		1	4	–	2.02	1.975	–	133.6 ± 0.3		3 ± 1			

[a] Z is the distance of samples from the top of the scarp. Z_E corresponds to an estimation of the sample depth before the scarp was exhumed (see text for explanations). S is the topographic shielding factor from *Dunne et al.* [1999]. T is the sample thickness. Sn and Sμ are the scaling factors for the neutrons and slow/fast muons, respectively.

[b] Internal uncertainties that include the counting statistics, the machine stability (~0.5%), and the blank correction whose ^{10}Be/^{9}Be ratio was 2.77 * 10^{-15} for this session.

[c] Values reported correspond to the inheritance obtained for surface denudation rates of 13 ± 2 mm ka^{-1}. Uncertainty of the surface denudation rate has been propagated in the calculation.

[d] Values reported are means of the inheritance obtained for surface denudation rates of 3 ± 1 mm ka^{-1} and 5 ± 1 mm ka^{-1}.

[e] Exposure ages are reported with internal uncertainties and external uncertainties (in parentheses), including the propagation of uncertainties related to the inheritance calculation.

[f] This sample was collected along the eroding bedrock slope, a few dozen of meters above the top of the scarp (see location Figures 2b and 3a and 3b) and is only used to calculate a maximum long-term denudation rate.

[g] These samples are recalculated from the database of *Hall et al.* [2008] to obtain comparative maximum long-term denudation rates.



Figure 5. Vertical offset of 1.5 m in an active channel along the Purgatorio Fault. Note that here the upstream block is uplifted (northern compartment). See picture location in Figure 4a.

concentration. Analytical and total uncertainties (1σ) are reported for each exposure age. Analytical age uncertainties include uncertainties in the measured ^{10}Be concentration (Table 1), sample thickness (±1 cm), bulk density (±0.2 g cm^{-3}), shielding factor (±0.02), and attenuation length (±10 gr cm^{-2}). Total age uncertainties include contributions from the analytical method and estimates of production rates [*Marrero et al.*, 2016]. All results are presented in Table 1.

4. Results and Discussion

4.1. Geomorphic Evidence of Recent Tectonic Deformation Along the Purgatorio Fault

Morphologies associated with recent fault activity are clearly visible in the hyperarid landscapes of this region of southern Peru (Figure 1). The overall E-W trace of the fault undulates slightly from NW-SE to SE-NW (Figure 1). Along its eastern segment, the fault intersects a dense network of intermittent fluvial channels, offering abundant evidence of recent vertical and right-lateral motion (Figure 2 and supporting information). The well-preserved near-vertical scarp is observed all along the fault trace in interfluves and shows a cumulative vertical offset of at least 5 m (Figures 3 and 4b). This cumulative vertical offset is certainly underestimated because of gravitational collapse affecting the upper scarp edge and accumulation of an unconsolidated colluvial wedge that covers the footwall (~1 m; Figures 3b and 4b). The fault scarp itself appears indurated and is sporadically covered by a thin (few centimeters) fault gouge composed of foliated red clays. It shows numerous cobbles that have been cut and striated with tectonic slickensides (Figure 4c).

As revealed by structural measurements (Figure 2a), the fault dip is always steep but oscillates between north and south dipping depending on location along the trace. We observed striations plunging 50 to 60° to the west, with markers of reverse motion (Figure 4c) coincident with locally folded layers (Figure 4d). Oscillation of the dip of the subvertical fault plane from north to south produces local inversions of the hanging wall and footwall, but in all cases, it corresponds to reverse faulting. For instance, between latitudes 70°35′30″W and 70°34′30″W, the fault orientation is 095/80 N (strike/dip angle and direction) (Figures 2a and 4a). Here the northern block corresponds to the hanging wall, which is uplifted with respect to the southern side (footwall). We note a striking difference between the local footwall erosional morphology with smooth and gentle slopes, while the hanging wall has a steeper and rougher topography (Figures 2b, 4a, and 5). Between latitudes 70°35′30″W and 70°37′30″W (Figure 2a), the situation is reversed: the fault orientation is 120/80S, making the local hanging wall the southern block and the footwall the northern block (Figure 6). Accordingly, the uplifted southern block is characterized by a higher degree of surface roughness (Figures 2b and 6a) that plausibly reflects a localized dynamic topographic response to the differential uplift experienced along each side of the fault. While local oscillations in fault plane dip occur along its ~60 km length, longer lived geomorphic features suggest that it is a west-vergent oblique (right-lateral) reverse fault associated with the flower structure of the Incapuquio Fault System. The Purgatorio Fault, which bounds the southern portion

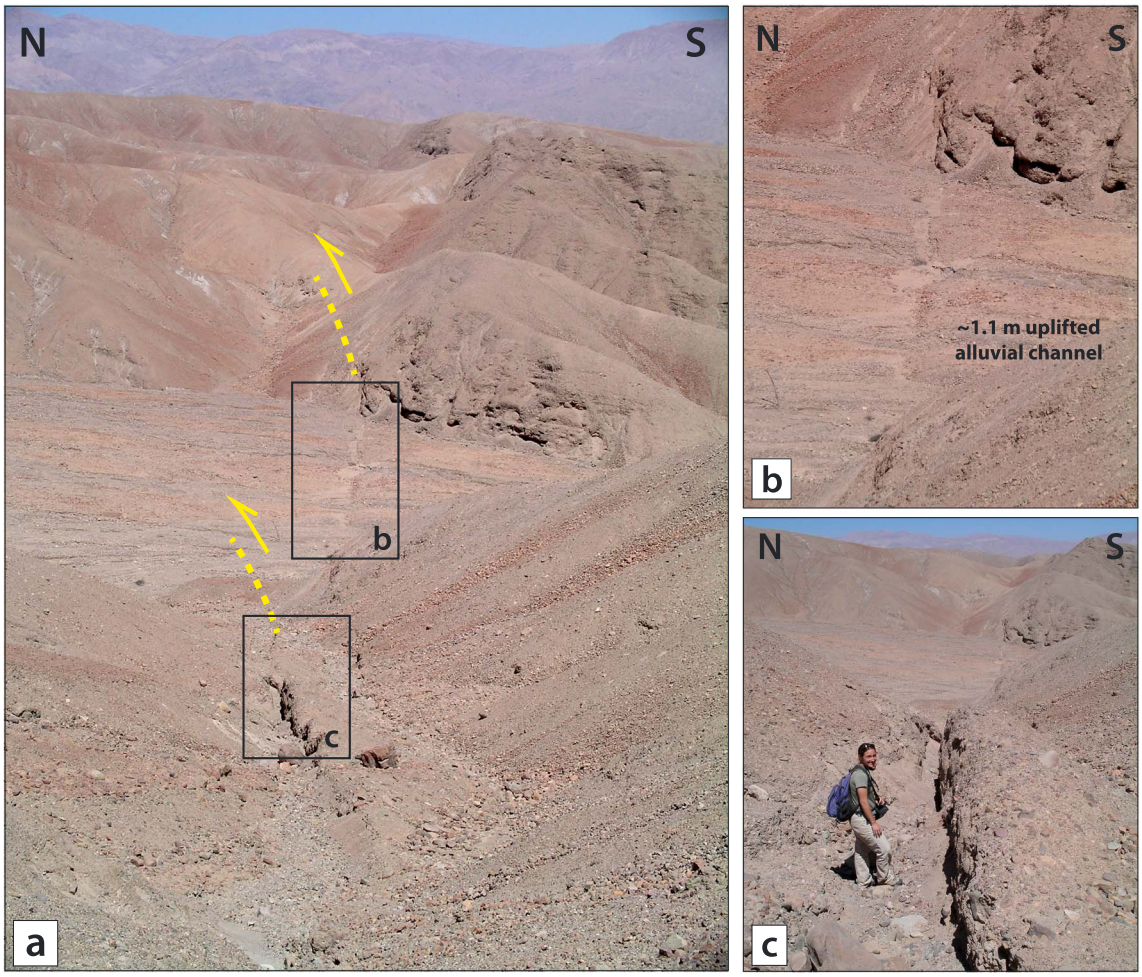


Figure 6. Imprints of the Purgatorio Fault in the arid Precordillera landscape. (a) Panoramic view. (b) Zoom on a vertical offset in an active channel. Note that here the downstream part is uplifted (southern compartment). (c) Zoom on the fault scarp. See zoomed pictures location in Figure 6a.

of an uplifted block of bedrock, is visible in the morphology as an abandoned and incised pediment surface stretching from the Rio Moquegua in the west to the Rio Locumba in the east and bound to the north by the Incapuquio Fault System (Figure 1). In the field, where the fault trace intersects dry channels and gullies, its polarity is confirmed by a vertical offset of ~1.5 m, which is recorded along the river channels (Figures 5 and 7a). Indeed, where the fault dips northward, the northern side of the river channels is uplifted relative to the southern portions (profiles 1, 2, and 3 on Figure 5a); the situation is reversed where the fault dips southward (profile 4 on Figure 5a). The uplifted alluvial beds near the fault plane were reincised by subsequent fluvial events, leaving small abandoned terraces that end abruptly at the fault scarp (Figures 4a and 5). Only 1 to 2 m of vertical offset is recorded in the river channels, compared to a cumulative vertical offset of several meters elsewhere along the fault trace (Figures 2 and 4b). This may indicate that the fault activated episodically and that its geomorphic imprint in the rivers and gullies was eroded by episodic fluvial erosion between successive tectonic events. If this interpretation is correct, the 1 to 2 m of vertical offset that is still visible in the river channels might represent the most recent rupture (Figures 2 and 4a).

Recent and small right-lateral offsets of about 3 to 4 m, which displace minor gullies and ridge crests, are also recorded along the fault trace (Figure 7b). These recent and easily erodible features are found along more than 30 km of the fault trace (supporting information) and are interpreted as cumulated from the last fault ruptures. Older and larger cumulative right-lateral offsets are also visible along the main ridge crests (Figure 2a), indicating a maximum of ~70 m of right-lateral cumulative displacement during the Holocene.

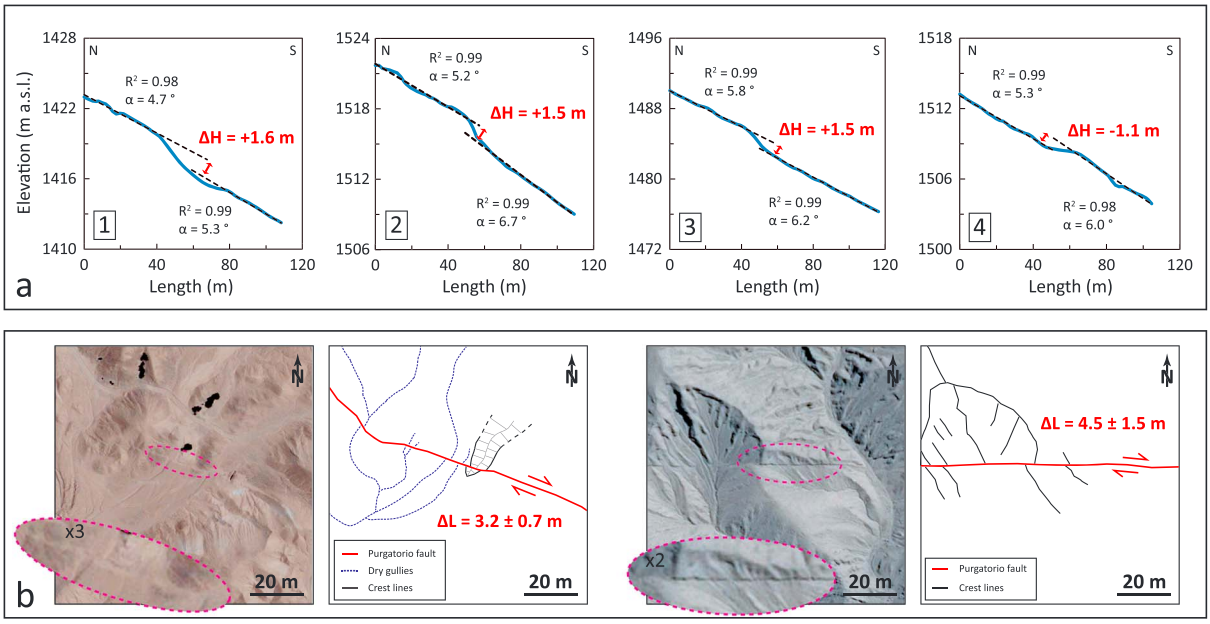


Figure 7. Offset morphological features along the Purgatorio Fault trace that are related to the last activity along the fault. (a) Vertical offsets (ΔH) along river channels revealed by topographic cross sections extracted from the Pléiades DEM (2 m resolution; see location in Figure 2). Profiles 1 and 2 correspond to sites shown on Figures 5 and 6b, respectively. (b) Examples of right-lateral offsets (ΔL) of gullies and interfluves crest lines revealed by high-resolution (70 cm) optical imagery (Google Earth, see location in the supporting information).

4.2. Denudation Rates, Inheritance, and Fault-Scarp Exposure Ages

4.2.1. Denudation Rates

The long-term denudation rate, calculated for sample F6 based on the measured ^{10}Be concentration, gives a maximum estimate for the denudation rate of the hanging wall (Figure 4a) of 13 ± 2 mm ka^{-1} (Table 1). For the footwall, maximum long-term denudation rates have been recalculated using 3 samples from *Hall et al.* [2008] (Figure 4a) and range from 3 ± 1 mm ka^{-1} to 5 ± 1 mm ka^{-1} (Table 1), giving a weighted-mean of 4 ± 1 mm ka^{-1}, i.e., about 3 times less than the denudation rate of the uplifted hanging wall. This is consistent with apparent surface roughness (Figure 2b) and the landscape morphology (Figures 4 and 6), both of which show higher denudation along the hanging wall block.

4.2.2. Inheritance Scenarios

Figure 8a shows the inheritance expected at depth, before scarp exhumation, for two different scenarios of long-term surface denudation. For comparison, the ^{10}Be concentrations measured at the surface and along the fault scarp are also plotted on the graph, according to their estimated depth (Z_E; preexhumation depth).

For scenario 1, applying the local denudation rate estimated in this study for the hanging wall block (ε = 13 ± 2 mm ka^{-1}), the calculated inheritance is found to be unexpectedly close to the measured ^{10}Be concentrations (Figure 8 and Table 1). This may imply very young exposure ages for the fault scarp. In this scenario, up to 90% of the concentrations measured along the fault scarp would have existed before exhumation (Table 1), and thus, only 10% was acquired by direct exposure. To account for denudation variability, we propagated the uncertainty associated with the denudation rate (ε = 13 ± 2 mm ka^{-1}) in the inheritance calculation. Overall, this uncertainty propagation has only a small effect on the inheritance, which varies by no more than 5% at the depth of the samples (Figure 8 and Table 1).

For scenario 2, in which we applied the local footwall denudation rate (ε = 3–5 mm ka^{-1}), we found that the calculated inheritance exceeds our measured ^{10}Be concentrations (Figure 8 and Table 1). This indicates that scenario 2 is not realistic.

4.2.3. Exposure Age and Purgatorio Fault Activity

Considering end-member scenario, the age of the PF scarp can be formerly bracketed between exposure ages calculated neglecting inheritance (the oldest) and exposure ages derived from scenario 1 (the youngest).

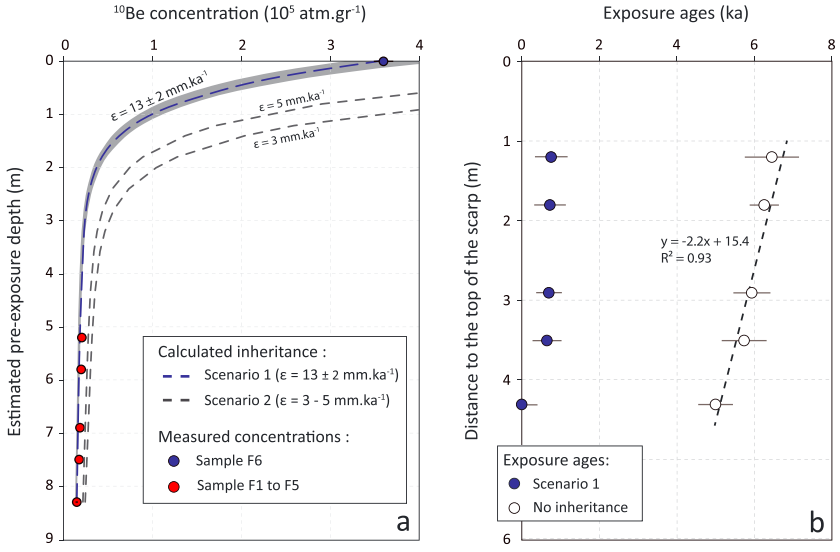


Figure 8. ^{10}Be cosmogenic nuclide concentration modeling results. (a) The dashed lines show theoretical evolution of the ^{10}Be inheritance expected at depth for different surface denudation rates. The shaded area around the curve of scenario 1 (ε = 13 ± 2 mm ka^{-1}) shows the propagation of denudation rate uncertainty on the inheritance calculation. The measured ^{10}Be concentrations of the samples from the fault scarp (F1 to F5) and the surface (F6) are plotted for comparison (see the text for details on their preexhumation depth estimation and inheritance calculation). (b) Corresponding ^{10}Be exposure ages obtained along the Purgatorio fault scarp for scenario 1. Note that scenario 2 is unrealistic (see text). Exposure ages calculated without inheritance are also reported for comparison.

Exposure ages calculated neglecting inheritance range from 5 to 6 ka (Table 1). In this interpretation, the PF might have crept or alternatively ruptured during multiple earthquakes, with a mean slip rate of 2.2 mm yr^{-1} (Figure 8b). However, in our opinion, these ages should be considered as extreme older bounds on the scarp age. Indeed, the high ^{10}Be concentrations measured at the surface (≥1 × 10^6 at g^{-1}), both here and in previous regional studies [e.g., *Hall et al.*, 2008; *Placzek et al.*, 2010], attest to long-term exposure and low-surface denudation of these landscapes, rendering the hypothesis of no inheritance at such shallow depth mostly unrealistic.

Based on scenario 1, which takes into account the measured denudation rate of the footwall block and its calculated associated inheritance and uncertainty propagation, exposure ages range from 0.2 ± 0.2 to 0.7 ± 0.5 ka (Table 1). The upper 3 m of the scarp yield exposure ages that are indistinguishable within their uncertainties, with a weighted mean of 0.7 ± 0.5 ka. The lowermost sample (F1), at the scarp base, shows a notably lower residual ^{10}Be concentration that results in a younger exposure age of 0.2 ± 0.2 ka (Figure 8b). It is important to notice that, under this scenario, the final ages are calculated from a small quantitative difference (~10%) between the modeled inheritance and the measured concentrations (Table 1). This might imply that a small shift of the modeled inheritance component would considerably change the final calculated exposure ages. Nevertheless, we emphasize that (1) the propagation of uncertainty on the inheritance model does not exceed 5% at the corresponding sample depths (Figure 8a and Table 1) and that (2) because the denudation rate measured at the scarp top corresponds to a maximum value, exposure ages even younger than those of scenario 1 would be expected in the case of underestimation of the inheritance.

Globally, these cosmogenic data indicate that the Purgatorio Fault has been active recently (late Holocene) or very recently (last few thousands of years). We admit that from these data alone, we cannot conclusively differentiate between multiple seismotectonic events and continuous creep. Indeed, given the uncertainty associated with the determination of inheritance, all of the samples could equally well record the same young age for the scarp. Nevertheless, geomorphic observations show that at least 5 m of cumulated vertical scarp are preserved along the interfluve landscapes, while only 1 to 2 m are observable across the river channels. This suggests (1) multiple and distinct tectonic events and (2) intermittent erosion phases in the rivers. Hence, coupling all the geomorphic observations with our preferred scenario 1, we propose an interpretation of at

least two successive events along the PF: (1) ~3 m of vertical coseismic displacement may have occurred at ~0.7 ka before being erased by a large flood event(s), followed by (2) another (most recent?) vertical offset of ~2 m developed along the fault trace during a second seismic event. Taking 60 km as the maximum length of the PF, about 60 km, and ~3 m of coseismic slip, a magnitude larger than M_w 7 could be expected for this area. An earthquake of this size would pose a significant hazard to local populations [*Wells and Coppersmith*, 1994]. An alternative interpretation is to consider multiple events of scarp exhumation. These would imply smaller offsets per event (i.e., smaller seismic magnitude) and a shorter recurrence time between each fault rupture.

Beyond the most recent activity on the fault, geomorphic observations permit us to assess its potential long-term activity. On its western termination, the PF intersects a shallow-dipping (<5°) abandoned pediment surface (100 m above the active channel north of the fault and 10 m above the channel south of the fault). The pediment surface, which was dated at ~ 300 ka by *Hall et al*. [2008], is vertically offset by at least 40 to 50 m. This value is consistent with the ~70 m of cumulative right-lateral offset recorded along the ridge crests (Figure 2a). The mean slip rates over this time span of 300 ka would thus be 0.15 to 0.2 mm yr^{-1} in the vertical and the horizontal directions, respectively. Both observations indicate that the PF has accumulated only a small amount of deformation (<100 m) over the long term, suggesting that it is a neotectonic structure that was activated at depth during the last few million years but reached the surface only in the Pleistocene-Holocene.

4.2.4. Climatic Implications on the Purgatorio Fault Rupture Chronology

Considering our dating results that formally bracket the Purgatorio Fault age between 0 and 6 ka, recent reworking of the river channels (i.e., younger than the top of the 5 m scarp) must be invoked to explain why the channels have recorded so little offset compared to the interfluves areas (see section 4.1). In general, such reworking seems plausible, as pointed out in *Lamb and Fonstad* [2010] or in *Storz-Peretz et al.* [2011], who have shown that the incision/erosion of tectonically uplifted zones in river beds can be extremely rapid, up to ~1 m/yr or even higher during a single large flood event. However, the river networks in the hyperarid Precordillera region are dry most of the time, except during exceptional El Niño events [e.g., *Keefer and Moseley*, 2003]. Thus, an important question is whether the young age for the channel deposits, implied by our data, is reasonable.

Throughout the hyperarid forearc region, evidence is found for large floods and debris flows that occurred during the Pleistocene-Holocene and were associated with El Niño events. This evidence includes preserved fluvial terraces and buried archeological sites [e.g., *Goldstein and Magilligan*, 2011; *Keefer and Moseley*, 2003; *Manners et al.*, 2007; *Goldstein and Magilligan*, 2011]. Radiocarbon chronologies from both coastal and Precordilleran sites suggest recurrence intervals for large El Niño-driven floods of <2500 years for the late Pleistocene, <600 years for the early Holocene, and <1500 years for the late Holocene [*Keefer and Moseley*, 2003]. *Goldstein and Magilligan* [2011] and *Manners et al.* [2007] found evidence of large floods along Rio Moquegua, such as the one associated with the 1997–1998 El Niño. These floods may induce channel widening of ~30 m, with floodplain erosion rates of 2 ha of land per kilometer of river, and have a recurrence interval of 50–100 years. Further, they suggest that in the Moquegua valley, ~80% of the floodplain has been modified/reworked during the last 550 ^{14}C years. This timing of flood recurrence appears fully consistent with our scenario.

While it is quite reasonable to expect large floods within the major canyons that are connected to the precipitation source in the high Andes, such events should be less common in small catchments within the hyperarid Precordillera region. However, *Goldstein and Magilligan* [2011] also show evidence for two severe floods in the Rio Muerto, a tributary to the Rio Moquegua that is not connected to high Andes precipitation sources. This tributary is located ~40 km west of our study area (see Figure 1) and has a drainage basin similar in size and catchment characteristics to those along the Purgatorio Fault (the highest portions of both catchments are at ~1500 m above sea level (asl)). On this site, *Magilligan and Goldstein* [2011] record large flood events associated with a Mega-Niño at 1300–1400 A.D. (Miraflores flood) and 700 A.D. It is thus plausible that the flood associated with the 1300–1400 A.D. Mega-Niño destroyed the fault scarp associated with the ~700 year rupture in the channels of the Purgatorio area, preserving evidence only for the most recent rupture event in the channels. Even this young event has been modified by subsequent fluvial activity because the uplifted terraces are abandoned and incised (Figures 4a and 5). Recent and smaller fluvial activities are also consistent with the results of *Goldstein and Magilligan* [2011], which record significant reworking of floodplains in the

last 300–350 years. To test the idea of recent fluvial reworking of the floodplain, additional sampling of the offset channel deposits for both OSL dating and ^{10}Be measurements is planned in the near future.

Overall, this young fault activity, the geomorphic evidence suggesting erosion of the penultimate tectonic scarps, and the regional climatic data suggesting occurrence of exceptional El Niño-driven flood events indicate that youthful and dynamic processes modified a generally ancient landscape.

4.3. Insights for the Active Deformation of the Peruvian Forearc

The present morphology of the Western Cordillera of the Central Andes is characterized by a large bend in the orogen, referred to as the Arica Bend. In the Central Andes, the thrusting propagated toward the western flank along the Western Cordillera during the Oligocene [*Victor et al.*, 2004; *Farías et al.*, 2005; *Roperch et al.*, 2006; *Armijo et al.*, 2015]. In southern Peru, the present-day deformation front along the Western Cordillera is represented by a large compressive flower structure that includes (1) left-lateral transpressional faults such as the Incapuquio Fault System [*Jacay et al.*, 2002] and (2) right-lateral transpressional faults, west-vergent thrusts, and blind thrusts marking the boundary between the western edge of the incised Precordillera and the low-relief Longitudinal Basin [*McCaffrey*, 1996; *Hall et al.*, 2012]. This study provides new evidence that this second type of contractile tectonic deformation was active in the Holocene and located in the Precordillera of the Western Cordillera. Our detailed analysis of a high-resolution DEM coupled with field mapping and new chronologic data demonstrates its youth, its transpressive right-lateral kinematics, its west-vergent geometry, and its eastern along-strike connection to the Incapuquio Fault System.

In the northern Chilean forearc, previous studies attributed reverse faults and folds to a flower structure that accommodates Andean contractional deformation on its western flank [*Victor et al.*, 2004; *Armijo et al.*, 2015]. At the Quaternary time scale, in contrast to the pure compression in Chile, a clear oblique component is distributed in the southern Peruvian forearc along the Purgatorio and Sama-Calientes faults [*Audin et al.*, 2008]. Similarly, the largest rotations derived from GPS data are observed in the forearc of southern Peru [*Bevis and Martel*, 2001; *Weiss et al.*, 2016]. Based on the comparison of real-time GPS data with paleomagnetic data, *Allmendinger et al*. [2005] proposed that some of the interseismic deformation field reflects permanent and long-term deformation of the upper plate. However, until this study, no data were available to interpret tectonic deformation during the Quaternary. Our results are compatible with strain partitioning in the southern Peruvian forearc resulting from increasing obliquity of plate convergence north of the Arica Bend [*Allmendinger et al.*, 2005].

In addition, our study is the first to provide *direct* quantitative constraints on the rate of deformation accommodated by a crustal-scale surface-breaking fault in the southern Peruvian forearc. Given the young ages presented here the limited amount of vertical deformation accommodated by the Purgatorio Fault during the late Quaternary (potentially $<$100 m during the last 300 ka) supports a neotectonic component of uplift along the Western Andean front [*Madella et al.*, 2016]. More regionally, longer (~2 Ma duration) forearc uplift rates of ~0.1–1 mm yr^{-1} were proposed by *Hall et al*. [2012, and references therein], but we demonstrate here that localized, meter-scale vertical and horizontal deformations occurred along individual reverse faults in the forearc during the last thousand years. Such results contrast with the first-order hypothesis of previous geodetic and modeling studies that assumed that tectonic strain of the forearc was time invariant and entirely elastic [*Villegas-Lanza et al.*, 2016]. To the contrary, in light of our findings, a significant amount of Holocene deformation could be accumulated on discrete faults within the forearc. This deformation should be taken in account in models of interseismic tectonic deformation across the Andean range (e.g., GPS coupling) [*Weiss et al.*, 2016].

5. Conclusions

Identification and description of active faults is needed to address seismic hazard issues and to understand the relationships between tectonic activity and relief generation. This applies especially to the Andean forearc of southern Peru, where the tectonic deformation has previously been investigated using only geological and structural mapping (Neotec Open database; http://neotec-opendata.com). In this paper, we present a detailed analysis of the Purgatorio Fault, an important active fault bounding the Precordillera of southwestern Peru. Based on field mapping, a high-resolution Pléiades digital elevation model (DEM), and direct cosmogenic radionuclide exposure dating (^{10}Be), we reach the following conclusions:

1. The Purgatorio Fault is a 60 km long right-lateral reverse fault oriented NW-SE to W-E, mainly subvertical at the surface but likely dipping east at depth and on it eastern end where it connects to the Incapuquio fault system.
2. Geomorphic evidence such as a free face, cumulated scarps, and multiple offsets of recent geomorphic features (gullies, river channels, and topographic crests) indicate that the fault was active in the recent past (thousands of years) and may have triggered historical earthquakes.
3. Cosmogenic radionuclide exposure ages obtained along a vertical profile formally date the exhumation along the fault scarp between 0 and ~6 ka depending on the inheritance model that is applied. Combining our preferred scenario of exposure with the geomorphic evidence, we propose an interpretation of at least two rupture events, each with ~3 and ~2 m of vertical offset, which may have occurred during the last thousand years. Based on the fault length, such ruptures may plausibly have caused a $>M_w$ 7 seismic event [*Leonard*, 2010]. Nevertheless, given the resolution of the method, an alternative sequence of multiple smaller events cannot be excluded.
4. The limited length of the long-term cumulative offsets recorded suggests that the Purgatorio fault is a neotectonic structure. We suggest that it was active only in the Quaternary or still later.

Acknowledgments
All the data used to perform this study are available in the paper (table) and in the supporting information. This research is part of the IRD-INGEMMET convenio and was financially supported by IRD and INGEMMET (Neotectonics program) and a grant from *Labex OSUG@2020* (Investissements d'avenir—ANR10 LABX56). We also thank FONDECYT, which funded part of the PhD of Carlos Benavente by contract 297-2014. The Astrium and the ISIS/CNES program provided the Pléiades images. The TCN measurements were performed at the ASTER AMS national facility (CEREGE, Aix en Provence), which is supported by the INSU/CNRS, the ANR through the "Projets thématiques d'excellence" program for the "Equipements d'excellence" ASTER-CEREGE action, and IRD. The authors acknowledge Peter van der Beek for his comments and advise on a previous version of this manuscript, Pascal Lacroix for his support during the Pléiades images processing, and Nicholas Arndt for English edits. This manuscript benefited of careful and thorough reviews and comments from Robin Lacassin, an anonymous reviewer, and Taylor Schildgen as Associate Editor.

References

Allmendinger, R. W., R. Smalley, M. Bevis, H. Caprio, and B. Brooks (2005), Bending the Bolivian orocline in real time, *Geology*, *33*(11), 905–908, doi:10.1130/G21779.1.

Alvarado, A., L. Audin, J. M. Nocquet, S. Lagreulet, M. Segovia, Y. Font, G. Lamarque, H. Yepes, P. Mothes, F. Rolandone, P. Jarrin, and X. Quidelleur (2014), Active tectonics in Quito, Ecuador, assessed by geomorphological studies, GPS data, and crustal seismicity, *Tectonics*, *33*, 67–83, doi:10.1002/2012TC003224.

Armijo, R., R. Lacassin, A. Coudurier-Curveur, and D. Carrizo (2015), Coupled tectonic evolution of Andean orogeny and global climate, *Earth Sci. Rev.*, *143*, 1–35, doi:10.1016/j.earscirev.2015.01.005.

Arnold, M., S. Merchel, D. L. Bourlès, R. Braucher, L. Benedetti, R. C. Finkel, and M. Klein (2010), The French accelerator mass spectrometry facility ASTER: Improved performance and developments, *Nucl. Instrum. Methods Phys. Res., Sect. B*, *268*(11), 1954–1959, doi:10.1016/j.nimb.2010.02.107.

Audin, L., G. R. Herail, R. Riquelme, J. Darrozes, J. Martinod, and E. Font (2003), Geomorphological markers of faulting and neotectonic activity along the western Andean margin, northern Chile, *J. Quat. Sci.*, *18*(8), 681–694, doi:10.1002/jqs.787.

Audin, L., C. David, S. Hall, D. Farber, and G. Hérail (2006), Geomorphic evidences of recent tectonic activity in the forearc, southern Peru, *Rev. Asoc. Geol. Argent.*, *61*(4), 545–554.

Audin, L., P. Lacan, H. Tavera, and F. Bondoux (2008), Upper plate deformation and seismic barrier in front of Nazca subduction zone: The Chololo fault system and active tectonics along the Coastal Cordillera, southern Peru, *Tectonophysics*, *459*(1–4), 174–185, doi:10.1016/j.tecto.2007.11.070.

Baize, S., L. Audin, T. Winter, A. Alvarado, L. Pilatasig Moreno, M. Taipe, P. Reyes, P. Kauffmann, and H. Yepes (2015), Paleoseismology and tectonic geomorphology of the Pallatanga fault (Central Ecuador), a major structure of the South-American crust, *Geomorphology*, *237*, 14–28.

Balco, G., J. O. Stone, N. A. Lifton, and T. J. Dunai (2008), A complete and easily accessible means of calculating surface exposure ages or erosion rates from 10 Be and 26 Al measurements, *Quat. Geochronol.*, *3*(3), 174–195, doi:10.1016/j.quageo.2007.12.001.

Benedetti, L., I. Manighetti, Y. Gaudemer, R. Finkel, J. Malavieille, K. Pou, M. Arnold, G. Aumaître, D. Bourlès, and K. Keddadouche (2013), Earthquake synchrony and clustering on Fucino faults (Central Italy) as revealed from in situ 36Cl exposure dating, *J. Geophys. Res. Solid Earth*, *118*, 4948–4974, doi:10.1002/jgrb.50299.

Benedetti, L. C., and J. Van Der Woerd (2014), Cosmogenic nuclide dating of earthquakes, faults, and toppled blocks, *Elements*, *10*(5), 357–361, doi:10.2113/gselements.10.5.357.

Bevis, M., and S. J. Martel (2001), Oblique plate convergence and interseismic strain accumulation, *Geochem. Geophys. Geosyst.*, *2*(8), 1033, doi:10.1029/2000GC000125.

Borchers, B., S. Marrero, G. Balco, M. Caffee, B. Goehring, N. Lifton, and J. Stone (2016), Geological calibration of spallation production rates in the CRONUS-Earth project, *Quat. Geochronol.*, *31*, 188–198, doi:10.1016/j.quageo.2015.01.009.

Bourles, D., G. M. Raisbeck, and F. Yiou (1989), 10Be and 9Be in marine sediments and their potential for dating, *Geochim. Cosmochim. Acta*, *53*(2), 443–452, doi:10.1016/0016-7037(89)90395-5.

Brown, E. T., J. M. Edmond, G. M. Raisbeck, F. Yiou, M. D. Kurz, and E. J. Brook (1991), Examination of surface exposure ages of moraines in Arena Valley, Antarctica using insitu produced 10Be and 26AL, *Geochim. Cosmochim. Acta*, *55*, 2269–2283.

Broxton M. J., and L. J. Edwards (2008), The Ames stereo pipeline: Automated 3D surface reconstruction from orbital imagery, In: Lunar and planet. sci. conf., vol 39, abstract 2419.

Chevalier, M. L., P. Tapponnier, J. Van der Woerd, F. J. Ryerson, R. C. Finkel, and H. Li (2012), Spatially constant slip rate along the southern segment of the Karakorum fault since 200 ka, *Tectonophysics*, *530*, 152–179, doi:10.1016/j.tecto.2011.12.014.

Chlieh, M., H. Perfettini, H. Tavera, J. P. Avouac, and D. Remy Nocquet J. M., Bonvalot S. (2011), Interseismic coupling and seismic potential along the Central Andes subduction zone, *J. Geophys. Res.*, *116*, B12405, doi:10.1029/2010JB008166.

Coudurier-Curveur, A., R. Lacassin, and R. Armijo (2015), Andean growth and monsoon winds drive landscape evolution at SW margin of South America, *Earth Planet. Sci. Lett.*, *414*, 87–99.

Dorbath, L., A. Cisternas, and C. Dorbath (1990), Assessment of the size of large and great historical earthquakes in Peru, *Bull. Seismol. Soc. Am.*, *80*(3), 551–576.

Dunai, T. J., G. A. G. López, and J. Juez-Larré (2005), Oligocene-Miocene age of aridity in the Atacama Desert revealed by exposure dating of erosion-sensitive landforms, *Geology*, *33*(4), 321–324, doi:10.1130/G21184.1.

Dunne, J., D. Elmore, and P. Muzikar (1999), Scaling factors for the rates of production of cosmogenic nuclides for geometric shielding and attenuation at depth on sloped surfaces, *Geomorphology*, *27*(1), 3–11, doi:10.1016/S0169-555X(98)00086-5.

Farías, M., R. Charrier, D. Comte, J. Martinod, and G. Hérail (2005), Late Cenozoic deformation and uplift of the western flank of the Altiplano: Evidence from the depositional, tectonic, and geomorphologic evolution and shallow seismic activity (northern Chile at 19°30′S), *Tectonics*, *24*, TC4001, doi:10.1029/2004TC001667.

Gosse, J. C., and F. M. Phillips (2001), Terrestrial in situ cosmogenic nuclides: Theory and application, *Quat. Sci. Rev.*, *20*(14), 1475–1560, doi:10.1016/S0277-3791(00)00171-2.

Goldstein, P. S., and F. J. Magilligan (2011), Hazard, risk and agrarian adaptations in a hyperarid watershed: El Niño floods, streambank erosion, and the cultural bounds of vulnerability in the Andean middle horizon, *Catena*, *85*(2), 155–167.

Hall, S. R., D. L. Farber, L. Audin, and R. C. Finkel (2012), Recently active contractile deformation in the forearc of southern Peru, *Earth Planet. Sci. Lett.*, *337*, 85–92, doi:10.1016/j.epsl.2012.04.007.

Hall, S. R., D. L. Farber, L. Audin, R. C. Finkel, and A. S. Mériaux (2008), Geochronology of pediment surfaces in southern Peru: Implications for Quaternary deformation of the Andean forearc, *Tectonophysics*, *459*(1), 186–205, doi:10.1016/j.tecto.2007.11.073.

Hetzel, R. (2013), Active faulting, mountain growth, and erosion at the margins of the Tibetan plateau constrained by in situ-produced cosmogenic nuclides, *Tectonophysics*, *582*, 1–24, doi:10.1016/j.tecto.2012.10.027.

Hindle, D., J. Kley, E. Klosko, S. Stein, T. Dixon, and E. Norabuena (2002), Consistency of geologic and geodetic displacements during Andean orogenesis, *Geophys. Res. Lett.*, *29*(8), 1188, doi:10.1029/2001GL013757.

Isacks, B. L. (1988), Uplift of the central Andean plateau and bending of the Bolivian Orocline, *J. Geophys. Res.*, *93*(B4), 3211–3231, doi:10.1029/JB093iB04p03211.

Jacay, J., T. Sempéré, L. Husson, and A. Pino (2002), *Structural Characteristics of the Incapuquio Fault System, Southern Peru*.

Jackson, J., J. F. Ritz, L. Siame, G. Raisbeck, F. Yiou, R. Norris, and E. Bennett (2002), Fault growth and landscape development rates in Otago, New Zealand, using in situ cosmogenic 10Be, *Earth Planet. Sci. Lett.*, *195*(3), 185–193, doi:10.1016/S0012-821X(01)00583-0.

Keefer, D. K., and M. E. Moseley (2003), A 38 000-year record of floods and debris flows in the Ilo region of southern Peru and its relation to El Niño events and great earthquakes, *Palaeogeogr. Palaeoclimatol. Palaeoecol.*, *194*(1), 41–77.

Kober, F., S. Ivy-Ochs, F. Schlunegger, H. Baur, P. W. Kubik, and R. Wieler (2007), Denudation rates and a topography-driven rainfall threshold in northern Chile: Multiple cosmogenic nuclide data and sediment yield budgets, *Geomorphology*, *83*(1), 97–120, doi:10.1016/j.geomorph.2006.06.029.

Lacroix, P. (2016), Landslides triggered by the Gorkha earthquake in the Langtang valley, volumes and initiation processes, *Earth Planets Space*, *68*(1), 1, doi:10.1186/s40623-016-0423-3.

Lal, D. (1991), Cosmic ray labeling of erosion surfaces: In situ nuclide production rates and erosion models, *Earth Planet. Sci. Lett.*, *104*(2–4), 424–439.

Lamb, M. P., and M. A. Fonstad (2010), Rapid formation of a modern bedrock canyon by a single flood event, *Nat. Geosci.*, *3*(7), 477–481, doi:10.1038/ngeo894.

Leonard, M. (2010), Earthquake fault scaling: Self-consistent relating of rupture length, width, average displacement, and moment release, *Bull. Seismol. Soc. Am.*, *100*(5A), 1971–1988, doi:10.1785/0120090189.

Lifton, N., T. Sato, and T. J. Dunai (2014), Scaling in situ cosmogenic nuclide production rates using analytical approximations to atmospheric cosmic-ray fluxes, *Earth Planet. Sci. Lett.*, *386*, 149–160, doi:10.1016/j.epsl.2013.10.052.

McCaffrey, R. (1996), Estimates of modern arc-parallel strain rates in fore arcs, *Geology*, *24*(1), 27–30.

Madella, A., R. Delunel, L. Audin, and F. Schlunegger (2016), Why is there no Coastal Cordillera at the Arica Bend (western Central Andes)?, *Basin Res.*, doi:10.1111/bre.12218.

Magilligan, F. J., and P. S. Goldstein (2001), El Niño floods and culture change: A late Holocene flood history for the Rio Moquegua, southern Peru, *Geology*, *29*(5), 431–434, doi:10.1130/0091-7613.

Manners, R. B., F. J. Magilligan, and P. S. Goldstein (2007), Floodplain development, El Niño, and cultural consequences in a hyperarid Andean environment, *Ann. Assoc. Am. Geogr.*, *97*(2), 229–249.

Marrero, S. M., F. M. Phillips, B. Borchers, N. Lifton, R. Aumer, and G. Balco (2016), Cosmogenic nuclide systematics and the CRONUScalc program, *Quat. Geochronol.*, *31*, 160–187, doi:10.1016/j.quageo.2015.09.005.

McGroder, M. F., R. O. Lease, and D. M. Pearson (2015), Along-strike variation in structural styles and hydrocarbon occurrences, Subandean fold-and-thrust belt and inner foreland, Colombia to Argentina, *Geol. Soc. Am. Mem.*, *212*, 79–113.

McQuarrie, N. (2002), Initial plate geometry, shortening variations, and evolution of the Bolivian orocline, *Geology*, *30*(10), 867–870, doi:10.1130/0091-7613.

Nishiizumi, K., M. Imamura, M. W. Caffee, J. R. Southon, R. C. Finkel, and J. McAninch (2007), Absolute calibration of 10 Be AMS standards, *Nucl. Instrum. Methods Phys. Res., Sect. B*, *258*(2), 403–413, doi:10.1016/j.nimb.2007.01.297.

Perea, H., P. M. Figueiredo, J. Carner, S. Gambini, and K. Boydell (2003), Paleoseismological data from a new trench across the el camp fault (Catalan coastal ranges, NE Iberian peninsula), *Ann. Geophys.*, *2003*.

Phillips, F. M., D. C. Argento, G. Balco, M. W. Caffee, J. Clem, T. J. Dunai, and A. T. Jull (2016), The CRONUS-Earth project: A synthesis, *Quat. Geochronol.*, *31*, 119–154, doi:10.1016/j.quageo.2015.09.006.

Placzek, C. J., A. Matmon, D. E. Granger, J. Quade, and S. Niedermann (2010), Evidence for active landscape evolution in the hyperarid Atacama from multiple terrestrial cosmogenic nuclides, *Earth Planet. Sci. Lett.*, *295*(1), 12–20, doi:10.1016/j.epsl.2010.03.006.

Riesner, M., R. Lacassin, M. Simoes, R. Armijo, R. Rauld, and G. Vargas (2017), Kinematics of the active West Andean fold-and-thrust belt (Central Chile): structure and long-term shortening rate, *Tectonics*, *36*, 287–303, doi:10.1002/2016TC004269.

Rocha, E., and E. O. Cristallini (2015), Controls on structural styles along the deformation front of the Subandean zone of southern Bolivia, *J. Struct. Geol.*, *73*, 83–96, doi:10.1016/j.jsg.2015.02.010.

Rolland, Y., C. Petit, M. Saillard, R. Braucher, D. Bourles, R. Darnault, and ASTER Team (2017), Inner gorges incision history: A proxy for deglaciation? Insights from cosmic ray exposure dating (10Be and 36Cl) of river-polished surfaces (Tinée River, SW Alps, France), *Earth Planet. Sci. Lett.*, *457*, 271–281.

Roperch, P., T. Sempere, O. Macedo, C. Arriagada, M. Fornari, C. Tapia, and C. Laj (2006), Counterclockwise rotation of late Eocene-Oligocene fore-arc deposits in southern Peru and its significance for oroclinal bending in the central Andes, *Tectonics*, *25*, TC3010, doi:10.1029/2005TC001882.

Saillard, M., S. R. Hall, L. Audin, D. L. Farber, V. Regard, and G. Hérail (2011), Andean coastal uplift and active tectonics in southern Peru: 10 Be surface exposure dating of differentially uplifted marine terrace sequences (San Juan de Marcona, ~15.4S), *Geomorphology*, *128*(3), 178–190.

Saillard, M., C. Petit, Y. Rolland, R. Braucher, D. L. Bourlès, S. Zerathe, and A. Jourdon (2014), Late Quaternary incision rates in the Vésubie catchment area (southern French alps) from in situ-produced 36Cl cosmogenic nuclide dating: Tectonic and climatic implications, *J. Geophys. Res. Earth*, *119*, 1121–1135, doi:10.1002/2013JF002985.

Saillard, M., L. Audin, B. Rousset, J.-P. Avouac, M. Chlieh, S. R. Hall, L. Husson, and D. L. Farber (2017), From the seismic cycle to long-term deformation: Linking seismic coupling and Quaternary coastal geomorphology along the Andean megathrust, *Tectonics*, *36*, 241, doi:10.1002/2016TC004156.

Schildgen, T. F., K. V. Hodges, K. X. Whipple, M. S. Pringle, M. Van Soest, and K. Cornell (2009), Late Cenozoic structural and tectonic development of the western margin of the central Andean plateau in southwest Peru, *Tectonics*, *28*, TC4007, doi:10.1029/2008TC002403.

Schlagenhauf, A., Y. Gaudemer, L. Benedetti, I. Manighetti, L. Palumbo, I. Schimmelpfennig, and K. Pou (2010), Using in situ chlorine-36 cosmonuclide to recover past earthquake histories on limestone normal fault scarps: A reappraisal of methodology and interpretations, *Geophys. J. Int.*, *182*(1), 36–72, doi:10.1111/j.1365-246X.2010.04622.x.

Sébrier, M., J. L. Mercier, F. Mégard, G. Laubacher, and E. Carey-Gailhardis (1985), Quaternary normal and reverse faulting and the state of stress in the central Andes of south Peru, *Tectonics*, *4*(7), 739–780, doi:10.1029/TC004i007p00739.

Sébrier, M., J. L. Mercier, J. Macharé, D. Bonnot, J. Cabrera, and J. L. Blanc (1988), The state of stress in an overriding plate situated above a flat slab: The Andes of central Peru, *Tectonics*, *7*(4), 895–928.

Storz-Peretz, Y., D. Bowman, J. B. Laronne, and T. Svoray (2011), Rapid incision of a small, coarse and steep fan-delta in response to base-level fall: The case of Nahal Qedem, the Dead Sea, Israel, *Earth Surf. Process. Landf.*, *36*, 467–480, doi:10.1002/esp.2066.

Uppala, S. M., P. W. Kållberg, A. J. Simmons, U. Andrae, V. D. Bechtold, M. Fiorino, and X. Li (2005), The ERA-40 re-analysis, *Q. J. R. Meteorol. Soc.*, *131*(612), 2961–3012, doi:10.1256/qj.04.176.

Uyeda, S., and H. Kanamori (1979), Back-arc opening and the mode of subduction, *J. Geophys. Res.*, *84*(B3), 1049–1061, doi:10.1029/JB084iB03p01049.

Victor, P., O. Oncken, and J. Glodny (2004), Uplift of the western Altiplano plateau: Evidence from the Precordillera between 20° and 21°S (northern Chile), *Tectonics*, *23*, TC4004, doi:10.1029/2003TC001519.

Villegas-Lanza, J. C., M. Chlieh, O. Cavalié, H. Tavera, P. Baby, J. Chire-Chira, and J.-M. Nocquet (2016), Active tectonics of Peru: Heterogeneous interseismic coupling along the Nazca megathrust, rigid motion of the Peruvian sliver, and Subandean shortening accommodation, *J. Geophys. Res. Solid Earth*, *121*, 7371–7394, doi:10.1002/2016JB013080.

Weiss, J. R., B. A. Brooks, J. H. Foster, M. Bevis, A. Echalar, D. Caccamise, and R. Smalley (2016), Isolating active orogenic wedge deformation in the southern Subandes of Bolivia, *J. Geophys. Res. Solid Earth*, *121*, 6192–6218, doi:10.1002/2016JB013145.

Wells, D. L., and K. J. Coppersmith (1994), New empirical relationships among magnitude, rupture length, rupture width, rupture area, and surface displacement, *Bull. Seismol. Soc. Am.*, *84*(4), 974–1002.

Zerathe, S., R. Braucher, T. Lebourg, D. Bourlès, M. Manetti, and L. Léanni (2013), Dating chert (diagenetic silica) using in-situ produced 10Be: Possible complications revealed through a comparison with 36Cl applied to coexisting limestone, *Quat. Geochronol.*, *17*, 81–93, doi:10.1016/j.quageo.2013.01.003.

Zerathe, S., T. Lebourg, R. Braucher, and D. Bourlès (2014), Mid-Holocene cluster of large-scale landslides revealed in the southwestern alps by 36Cl dating. Insight on an alpine-scale landslide activity, *Quat. Sci. Rev.*, *90*, 106–127, doi:10.1016/j.quascirev.2014.02.015.